frontiers | Frontiers in Marine Science

TYPE Original Research
PUBLISHED 25 November 2024
DOI 10.3389/fmars.2024.1499002

OPEN ACCESS

EDITED BY
Meilin Wu,
Chinese Academy of Sciences (CAS), China

REVIEWED BY
Xiaoteng Shen,
Hohai University, China
Zeng Zhou,
Hohai University, China

*CORRESPONDENCE
Leiping Ye
yeleiping@mail.sysu.edu.cn
Jiaxue Wu
wujiaxue@mail.sysu.edu.cn

RECEIVED 20 September 2024
ACCEPTED 04 November 2024
PUBLISHED 25 November 2024

CITATION
Lin Y, Ye L, Li C, Cui Y and Wu J (2024) Morphology and distribution of suspended particles during typhoon-induced algal bloom in the Pearl River Estuary.
Front. Mar. Sci. 11:1499002.
doi: 10.3389/fmars.2024.1499002

Morphology and distribution of suspended particles during typhoon-induced algal bloom in the Pearl River Estuary

Yaokun Lin[1], Leiping Ye[1*], Chao Li[1], Yongsheng Cui[2] and Jiaxue Wu[1*]

[1]School of Marine Sciences, Sun Yat-sen University and Southern Marine Science and Engineering Guangdong Laboratory (Zhuhai), Zhuhai, China, [2]Guangdong Center for Marine Development Research, Guangzhou, China

Suspended particles, including plankton and clay minerals, are ubiquitous in aquatic environments. Understanding their characteristics is crucial for gaining insights into biogeochemical processes and accurately assessing material and element fluxes in coastal estuaries. Following the impact of Typhoon Cempaka on the Pearl River Estuary (PRE) in July 2021, we conducted field observations throughout various stages of the subsequent algal bloom, simultaneously capturing holographic images of particles alongside hydrographic data. We developed an innovative method to transform these images into datasets for deep learning object detection models, enabling advanced morphological analysis. This approach allowed for efficient identification and characterization of particle morphology and vertical distribution in coastal estuarine environments. Our study revealed substantial morphological and distributional differences in diatoms and aggregates in response to environmental changes throughout the stages of the typhoon-induced algal bloom. Specifically, elongated-curled diatoms tended to settle in the middle and bottom layers under turbulent mixing but remained concentrated in the surface phytoplankton layer under stratified conditions. In contrast, short-straight diatoms exhibited minimal sensitivity to physical dynamics, persisting in the surface layer across all conditions. We observed that aggregate morphology and distribution patterns correlated with physical dynamics intensity and diatom concentration. These findings accurately reflect particles' natural states and underscore the potential of *in situ* particle morphology and distribution as indicators of environmental changes, highlighting the ecological significance of studying *in situ* particle functional traits. We recommend that future studies expand particle imaging across diverse conditions to deepen understanding of estuarine ecosystem evolution.

KEYWORDS

suspended particles, holography, typhoon, objects detection, algal blooms, Pearl River Estuary

1 Introduction

The term "marine particles" encompasses a wide variety of components in aquatic environments, including both coastal waters and open oceans. These particles consist of living organisms like zooplankton and phytoplankton, biotic detritus such as algal aggregates and fecal pellets, as well as non-living materials like suspended sediments and clay minerals (Kiko et al., 2022). Whether biotic or abiotic, these morphologically diverse particles play a crucial role in the global carbon cycle across aquatic ecosystems (Briggs et al., 2020; Worden et al., 2015). Phytoplankton, as a key living particle, contribute significantly to the carbon cycle through photosynthesis, serving as a primary source of organic carbon (Chavez et al., 2011). This organic matter transforms through food webs, flocculation, and bacterial decomposition, influencing carbon transport and deposition (Stemmann and Boss, 2012). Particle traits, including size, shape, and porosity, are crucial for understanding their dynamics, such as formation, sinking, and degradation (Boyd et al., 2019). Thus, detecting and analyzing particles is essential for studying carbon cycling and broader oceanic biogeochemical processes.

High-quality imaging is essential for obtaining detailed information on particle morphology, and extensive research has been conducted on morphological traits derived from such images (Orenstein et al., 2022). Morphological traits, which are specific attributes inherent to an individual, are often referred to as "functional traits" (Martini et al., 2021; Violle et al., 2007). For instance, traits like size, shape, and structure in diatoms transcend taxonomic boundaries, offering insights into how biological communities respond to environmental conditions. Analyzing these functional traits enables a quantitative assessment of phytoplankton communities' or ecosystems' resilience to environmental changes (Mcgill et al., 2006). Laboratory research has shown that diatoms are not merely passive particles in aquatic environments; their morphology reflects active responses to fluctuating external conditions. Under varying turbulence intensities, diatoms adjust their survival strategies, resulting in distinct adaptive morphologies (Sengupta et al., 2017). Furthermore, recent findings reveal that diatoms undergo genetic changes in response to environmental variability, underscoring their adaptive capabilities (Amato et al., 2017). However, while laboratory research has provided valuable insights, many of these findings regarding algae have yet to be fully validated in natural settings (Johnson et al., 2006; Moran et al., 2004). To address this gap, advances in statistical classification of image-based morphologies have enabled the identification of functional traits in natural aggregates. For example, Trudnowska et al. (2021) employed principal component analysis on a large dataset of *in situ* marine snow images from the Arctic, devising a method to assess and compare snow morphology across systems. This approach has been instrumental in evaluating carbon fluxes during algal blooms in ice-covered areas. These findings underscore the critical research value of *in situ* particle morphology and distribution, particularly in relatively stable environments like the Arctic. Nevertheless, understanding how these dynamics manifest in more complex and rapidly evolving ecosystems, such as densely populated coastal estuaries, remains limited. The morphology and distribution of particles in such environments are heavily influenced by both natural processes and anthropogenic factors, making them more challenging to study. In particular, the coupling of physical dynamics and particle morphology during post-typhoon algal blooms presents an area of crucial importance for environmental health monitoring, yet it remains relatively underexplored.

Underwater holographic imaging offers the capability to collect *in situ* particle data with high spatiotemporal resolution, owing to its flexibility in deployment. However, challenges in data reconstruction and the extraction of vast amounts of particle parameters have hindered the technology from reaching its full potential (Nayak et al., 2021). Fortunately, recent advancements in the YOLO (You Only Look Once) series of object detection models have enabled the automation of tasks such as object detection, classification, and feature extraction, standing out for their speed and accuracy (Terven et al., 2023). If applied to particle images, these technologies could significantly enhance the ability to detect, classify, and extract morphological traits from large collections of such images. Furthermore, by integrating pattern recognition, artificial intelligence, and machine learning, the automation of particle identification holds the potential to transform this specialized field into a more accessible and verifiable science (MacLeod et al., 2010). Incorporating object detection models into holographic image processing can generate a wealth of comprehensive data, allowing for the extraction of more intricate morphological traits. This, in turn, would enable a more detailed study of particle morphology and distribution from an *in situ* perspective.

Algal blooms in coastal oceans have intensified in recent years, drawing increasing attention (Dai et al., 2023). Typhoons have played a critical role in this process by facilitating vertical nutrient transport through upwelling and increasing nutrient inputs from subsequent runoff (Pan et al., 2017). The influx of freshwater and altered hydrodynamics following a typhoon significantly impacts the concentration and distribution of particles in the water, leading to complex physical-biogeochemical processes. Detecting rapid, short-term *in situ* changes induced by typhoons remains challenging, yet it is essential for effectively managing and forecasting the ecological health of estuarine environments. In this study, we utilized *in-situ* holographic imaging data, combined with object detection models, to develop algorithms capable of detecting, classifying, and quantifying particle morphology. Furthermore, we evaluated the broader applicability of this method in ecological research and, using *in-situ* particle statistics, conducted a quantitative assessment of the typhoon's impact on the coastal ecosystem.

2 Materials and methods

2.1 Study area and field observation

The Pearl River Estuary (PRE) is located in the northern South China Sea (Figure 1A). In July 2021, Typhoon Cempaka passed near the PRE, triggering an algal bloom. Leveraging this event, our study investigated particle dynamics during the bloom through field observations conducted immediately after the typhoon's landfall. The observation site (Site S, marked by a blue star in Figure 1A) is

situated in the transitional zone between the estuarine mouth and the shelf sea at a depth of approximately 15 meters, where both tidal and runoff dynamics exert influence. We conducted two consecutive 48-hour mooring observations at site S on the 3rd and 10th days following the typhoon's landfall, corresponding to the early bloom stage (Stage E: Jul. 23, 2021, 17:00 - Jul. 25, 2021, 17:00, Figure 1B) and the late bloom stage (Stage L: Aug. 1, 2021, 11:00 - Aug. 3, 2021, 11:00, Figure 1C). We used two survey modes during these observations. The first was hourly profiling, where instruments descended from the surface to the seafloor at 0.3 m s^{-1}, ensuring accurate particle distribution data across the vertical profile. The second involved continuous monitoring with a bottom-mounted platform, positioning instruments 0.6 m above the seafloor (Figure 1D). For profiling observations, we utilized a combination of instruments to collect vertical CTD (conductivity, temperature, depth) data, chlorophyll-a (Chl-a) concentrations, and holographic images of particles. These included an RBR-CTD, an SBE 25plus Sealogger CTD, and a LISST-HOLO2. A bottom-mounted platform was equipped with an ADV and an additional RBR-CTD to measure turbulent kinetic energy dissipation rates and CTD data near the seafloor. Additionally, we collected several *in situ* water samples at various times and depths, capturing particle images using an onboard Olympus X71 microscope. Detailed information on the instruments is provided in Supplementary Table 1.

2.2 Generating the composite focused images

The LISST-HOLO2 is a submersible digital holographic camera designed to capture holograms of suspended particles like plankton and aggregates, with a high sampling rate and fast data transmission, ideal for field observation (more details, see https://www.sequoiasci.com/). To mitigate poor image quality in high-turbidity environments (Choi et al., 2021), we equipped the device with an optical path reduction module to obtain clearer images. The field of view of the holograms is cropped to 1200 × 1200 $pixels^2$, with a resolution of 4.4 μm per pixel, and the reconstruction distance within the imaging sampling volume is 5 mm. Consequently, the imaging sampling volume of each hologram is approximately $V_{holo} = 1.39 \times 10^{-7}\ m^3$. Processing the holograms into a composite focused image (CFI) involves four main steps: raw hologram selection, preprocessing, reconstruction, and image plane consolidation (Figure 2A). To avoid invalid images from air exposure, we manually filtered the data, retaining around 92,000 high-quality holograms (Figure 3A). These high-quality holograms were then preprocessed by extracting the average of all images in a profile to create a background image (Figure 3B). Subtracting this background from each hologram effectively removed fixed spots on the lens and background noise (Nayak et al., 2018). The enhanced images (Figure 3C) were reconstructed within the imaging sampling volume using the angular spectrum method (De Nicola et al., 2005). We divided the imaging volume into 50 equal segments, with a reconstruction interval of 0.1 mm. As shown in Figure 2A, Z_i, Z_j, and Z_k represent different reconstruction distances within the sampling interval. In this study, we designed an overlapping sliding window algorithm, where a sliding window of 100 pixels in length moves with a stride of 50 pixels. We calculated the average edge Gaussian gradient value within the same sliding window position in each reconstructed image. The position at which this value reaches its maximum across different focal planes indicates the optimal focus distance for that sliding window (Liu et al., 2023). These focused sliding windows were then projected and consolidated onto a single plane to form a CFI. The targets in the

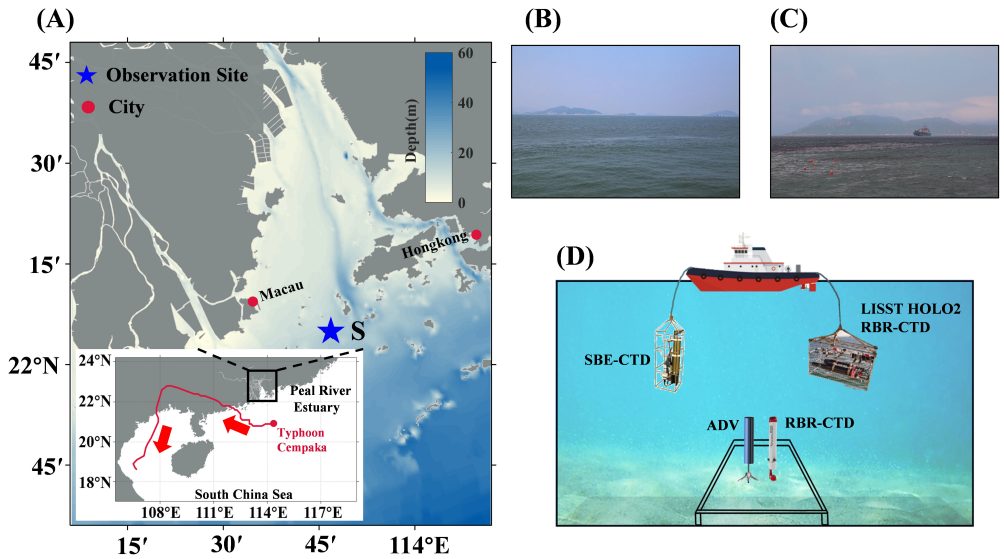

FIGURE 1
(A) Location of the Pearl River Estuary and the trajectory of Typhoon Cempaka. **(B, C)** Field photographs taken at site S during the early (Stage E) and late (Stage L) stages of the typhoon-induced algal bloom, illustrating the shift in water color from blue-green to dark brown or reddish-brown, respectively. **(D)** Schematic diagram of the instrument setup deployed for consecutive observation at mooring site S.

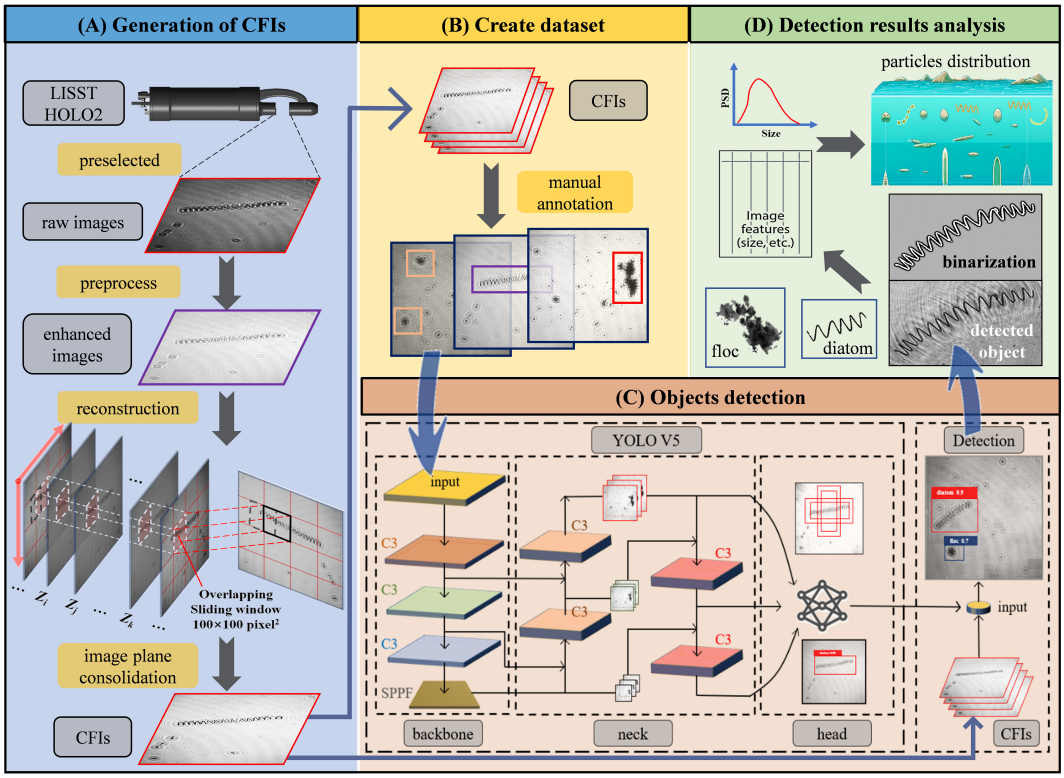

FIGURE 2
The workflow for acquiring and analyzing particle morphology and distribution information includes the following steps: **(A)** The process starts with the generation of composite focused images (CFIs), detailing the steps involved in converting raw holograms into CFIs. **(B)** A subset of the CFIs generated in step **(A)** is selected for manual annotation, which is then used to create a training dataset. **(C)** The YOLOv5x architecture, adapted from Jocher et al. (2022), is then used to train on the annotated dataset from step **(B)**, facilitating particle detection. **(D)** The final step involves further analysis of the detected particles, including binarization of the target images, extraction of morphological features, and reconstruction of distribution patterns.

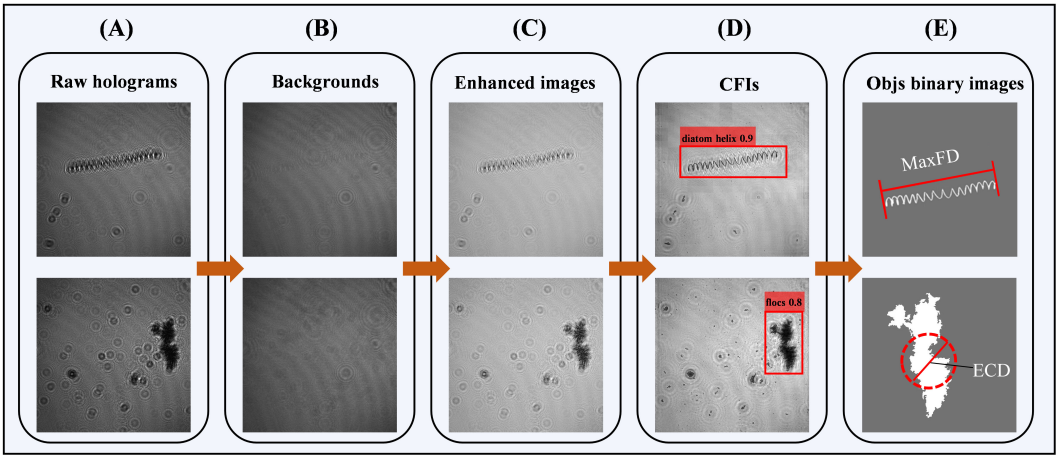

FIGURE 3
Main steps for generating composite focused images (CFIs) using two particle types: **(A)** Original holograms displaying clear interference fringes, noise, and uneven illumination; **(B)** Background extracted from profile data; **(C)** Enhanced images produced by background subtraction and denoising; **(D)** CFIs created via reconstruction and image plane consolidation, showing clear target contours; **(E)** Binarized images of detected target particles, with regions of interest extracted from CFIs in **(D)** are using a custom binarization algorithm. Two morphological parameters shown: MaxFD (maximum Feret diameter) for a helical diatom and ECD (equivalent circular diameter) for a floc.

CFI are generally clear and complete, allowing us to manually select and label them using annotation software (Figures 2B, 3D).

2.3 Creating the training dataset

A preliminary visual assessment of all the CFIs revealed that the algal bloom, observed throughout the entire observation period, was predominantly composed of diatoms. Biologically mediated aggregates primarily consisted of algal agglomerates and clay mineral flocs. The morphology of the diatoms was highly distinctive, presenting various curvilinear forms, including bead-string, chain-like, coiled, helical, and semicircular shapes. In contrast, the aggregates exhibited varying porosity and continuously changing shapes. Based on these morphological characteristics, we classified the particles in the CFIs into seven classes: (1) agglomerates, characterized by an aggregated morphology, where numerous small particles or filamentous structures cluster together to form larger clumps. Some portions may appear amorphous and irregular, lacking specific shape or structure, and presented a relatively loose and disorganized appearance (Figures 4A, 5A); (2) diatom beads, distinguished by small cells with transparent connections between them, resulting in a bead-string appearance as the connections are not clearly visible in the CFIs (Figures 4B, 5B); (3) diatom chain, which appear as relatively straight, solid chains, with the connections between diatom cells remaining dense after holographic imaging, although the chains may vary in thickness (Figures 4C, D, 5C); (4) diatom coiled, which feature chains of varying filament lengths that overlap like coiled ropes (Figures 4E, 5D); (5) diatom helix, characterized by elongated chains that bend and extend in a helical shape in space (Figures 4F, 5E); (6) diatom semicircle, forming an incomplete curve that resembles a C-shaped semicircle (Figures 4G, 5F); and (7) flocs, primarily composed of biologically mediated flocculated clay minerals, appearing as dense, complex structures with irregular, shifting boundaries (Figures 4H, 5G). Following these preliminary analyses, we preselected 5,430 images from the CFIs as the training dataset (Figure 2B). The images were carefully selected to include a variety of clear targets, ensuring sufficient samples for each class label. Approximately 10,000 targets, randomly distributed throughout the images, were manually labeled using the image labeler application. For a detailed overview, refer to Supplementary Figures 1, 2.

2.4 Objects detection

We selected YOLOv5 for our object detection model, first released by Ultralytics in 2020 and continually optimized (Jocher et al., 2022). Built on the PyTorch framework, YOLOv5 benefits from a robust ecosystem, making it ideal for object detection (Terven et al., 2023). Its architecture comprises three main components: backbone, neck, and head (Figure 2C). The backbone uses CSPDarknet53, integrating CSPNet (Wang et al., 2020) and Darknet53 (Redmon and Farhadi, 2018), with C3 convolutional modules for multi-scale feature extraction and an SPPF (Spatial Pyramid Pooling Fast) layer to pool features into a fixed-size map (Figure 2C). The neck includes a Feature Pyramid Network (FPN) (Liu et al., 2018) and a Path Aggregation Network (PAN) (Lin et al., 2017), enhancing feature fusion. FPN applies a top-down strategy for high-level feature integration, while PAN improves small object detection by merging features across multiple pathways. The neck generates three feature map scales that are passed to the head for prediction. The head generates predictions using anchor boxes and employs a loss function and non-maximum suppression (NMS) (Neubeck and Van Gool, 2006). The loss function combines binary cross-entropy for classification and confidence (Ho and Wookey, 2020) with CIoU loss for precise bounding box regression (Zheng et al., 2020). NMS eliminates redundant bounding boxes, retaining only the highest-probability box for final output. This process results in the final prediction,

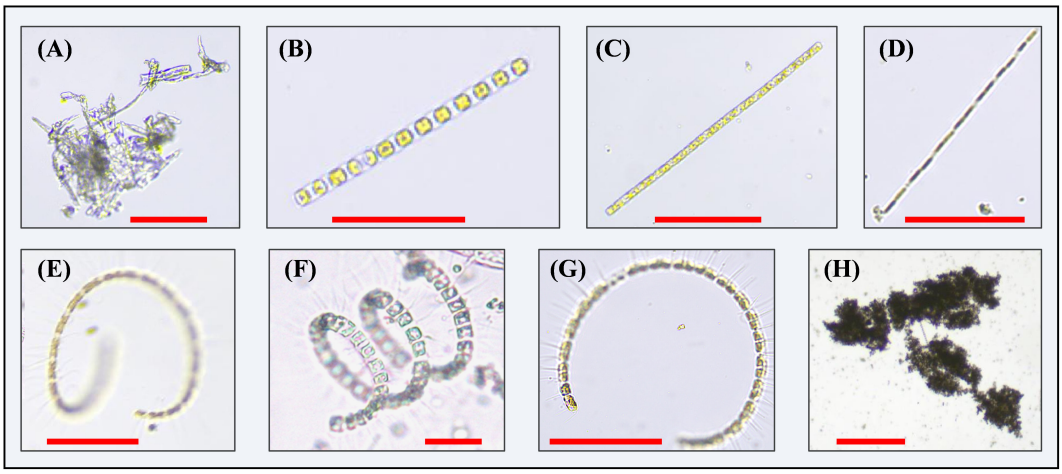

FIGURE 4
Main types of particles observed in water samples collected *in situ* during the observation period through microscopy: **(A)** Algal agglomerates, exhibiting a loose and irregular clustered state; **(B)** Bead string diatom; **(C)** Straight-chain diatom; **(D)** Thin filamentous diatom; **(E)** Coiled diatom; **(F)** Helical diatom; **(G)** Semicircular diatom; **(H)** Clay mineral floc. Red scale bars in all the panels represent 100 µm.

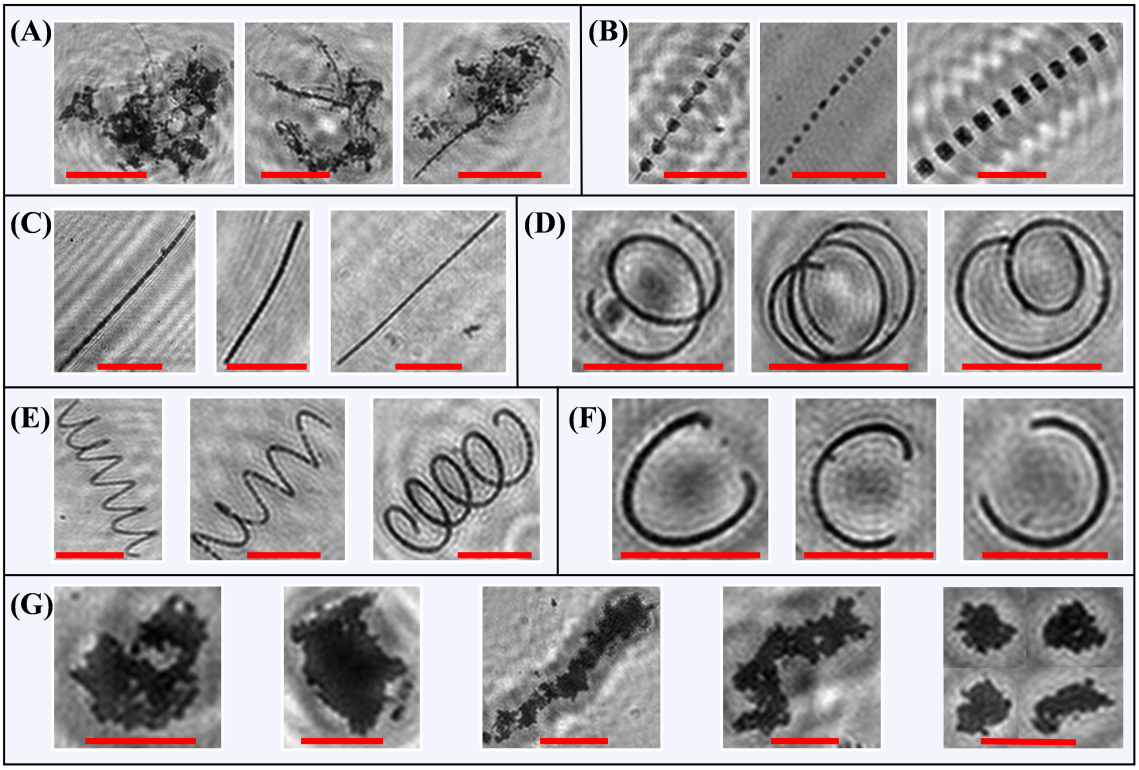

FIGURE 5
Examples of cropped images extracted from the composite focused images under different class labels: **(A)** agglomerates; **(B)** diatom beads; **(C)** diatom chain; **(D)** diatom coiled; **(E)** diatom helix; **(F)** diatom semicircle; and **(G)** flocs. Red scale bars in all the panels represent 100 µm.

which includes the object's class, score, and bounding box coordinates (Figure 2C). YOLOv5 introduces depth_multiple and width_multiple scaling factors to adjust layer count and channel size (Jocher et al., 2022). The five variants—YOLOv5n, YOLOv5s, YOLOv5m, YOLOv5l, and YOLOv5x—share the same architecture but differ in size. Smaller models like YOLOv5n prioritize speed for mobile use, whereas larger ones like YOLOv5x offer better performance with higher computational costs. This scalability allows YOLOv5 to balance speed and accuracy for various applications.

In this study, we chose YOLOv5x for higher detection precision, despite the increased computational cost. The dataset created in Section 2.3 was divided into training, testing, and validation sets in a ratio of 7:2:1. To evaluate the model's performance, we employed Recall (R), Precision (P), and Mean Average Precision (mAP) as the primary metrics. Recall measures the model's ability to correctly identify positive samples, while Precision indicates the accuracy of the model in classifying these positive samples (Padilla et al., 2020). The specific formulas for these metrics are as follows:

$$R = \frac{TP}{TP+FN} \times 100\,\% \tag{1}$$

$$P = \frac{TP}{TP+FP} \times 100\,\% \tag{2}$$

where TP (True Positive) represents the number of correctly identified positive samples, FP (False Positive) denotes the number of negative samples incorrectly classified as positive, and FN (False Negative) indicates the number of positive samples that were wrongly classified as negative. The determination of positive and negative samples is based on the Intersection over Union (IoU) threshold. The IoU is calculated as the overlap area between the predicted bounding box and the ground truth, divided by the area of their union. A sample is classified as positive if its IoU exceeds the threshold, otherwise, it is classified as negative.

Average Precision (AP) is a measure that integrates both recall and precision for ranked retrieval outcomes, providing an overall assessment of object detection performance. By plotting the Precision-Recall (P-R) curve, with P on the y-axis and R on the x-axis, the area under this curve represents the AP. The formulas for AP and mean Average Precision (mAP) are as follows:

$$AP = \int_0^1 P \cdot RdR \tag{3}$$

$$mAP = \frac{1}{N}\sum_{i=1}^{N} AP_i \tag{4}$$

where $N = 7$ is the number of classes in the dataset. At an IoU threshold of 0.5, the average precision of the model is denoted as AP0.5, and the mean average precision is denoted as mAP0.5. The mAP0.5 represents the mean average precision when the IoU threshold is 0.5. Additionally, mAP 0.5:0.95 is the average mAP

over IoU thresholds ranging from 0.5 to 0.95. These metrics, mAP 0.5 and mAP 0.5:0.95, are crucial for evaluating the algorithm's positional accuracy in target detection. By analyzing these values, one can gain a comprehensive understanding of the algorithm's detection performance across various targets.

2.5 Detection results analysis

All CFIs from Section 2.2 were input into the trained object detection model (Section 2.4) to identify particle targets, assign classes, and determine locations. Since class and bounding box data alone don't fully capture morphological details, each particle was extracted from its bounding box and converted into cropped images for further analysis (Figure 2D). We enhanced the segmentation algorithm based on the Expectation-Maximization method (Diplaros et al., 2007), which facilitated the acquisition of higher-quality binarized images (Figure 6, second row). Additionally, we introduced a new algorithm for calculating morphological parameters in various particles, enabling the effective extraction of these parameters from binarized images across different particle types.

For diatoms classes, some binary images displayed fragmented components, such as diatom beads (Figure 6A). To address this, we first connected these fragments belonging to the same particle within the cropped image using a proximity-based connection algorithm, and then applied skeletonization morphological operations to the entire binarized image. The skeleton image, being a single-pixel-wide representation, allowed us to calculate the number of pixels in the skeleton to represent the filament length (FL) of the diatom (Figure 6, third row). Given the varying sizes and morphologies of diatoms observed in this study, using FL as a representative morphological parameter is both reasonable and effective. For the complex curved morphologies of diatoms, we employed the coiling ratio (CR) to describe this attribute:

$$CR = \frac{maxFD}{FL} \tag{5}$$

where *maxFD* represents the maximum Feret diameter of the particle measured on the binarized image. The maximum Feret diameter is defined as the greatest distance between any two parallel tangents to the boundary of the particle within the image, representing the longest caliper measurement of the particle across all possible orientations (Figure 3E). A smaller CR indicates a higher degree of coiling, providing a comprehensive metric for quantifying the diatom morphology.

For agglomerates and flocs, we defined two additional parameters to describe their characteristics: the equivalent circular diameter (ECD) and the perimeter-based two-dimensional fractal dimension (DF2) (Maggi et al., 2006; Vahedi and Gorczyca, 2011). These parameters are calculated as follows:

$$ECD = \sqrt{\frac{4A}{\pi}} \tag{6}$$

$$DF2 = 2\frac{lg(P)}{lg(A)} \tag{7}$$

where A is the area of the particle and P is its perimeter. These values can be directly obtained by counting the total number of pixels and edge pixels in the binarized image. ECD effectively describes the size of the particle, while DF2 reflects the compactness and internal spatial structure of the particle. A

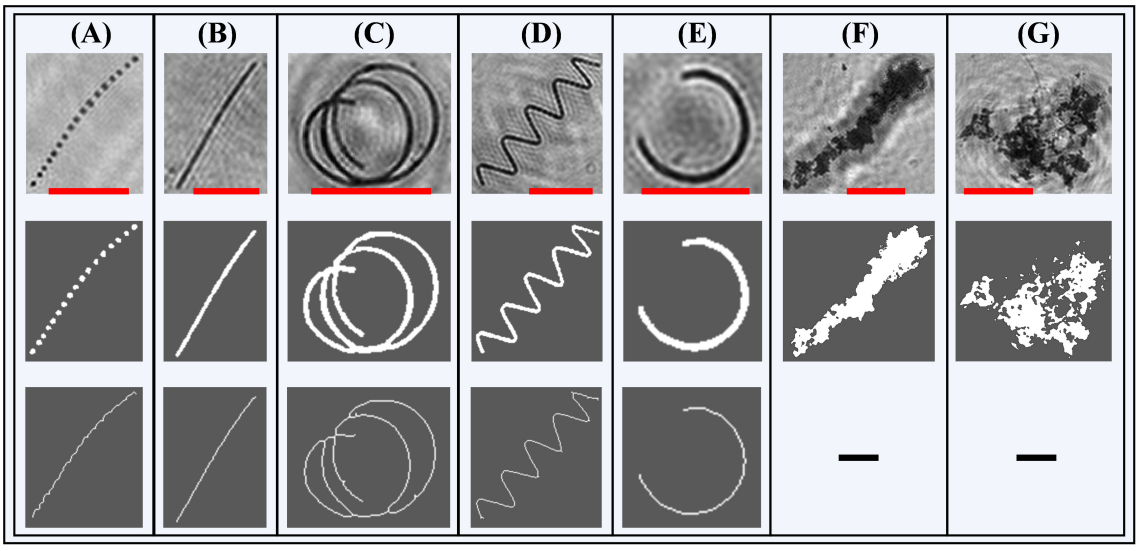

FIGURE 6
Examples of cropped images of various particles and their binarization and skeletonization: **(A)** diatom beads, **(B)** diatom chain, **(C)** diatom coiled, **(D)** diatom helix, **(E)** diatom semicircle, **(F)** flocs, **(G)** agglomerates. The first row shows particle images cropped from composite focused images using bounding box data from the object detection model. The second row displays the binarized images, and the third row shows the corresponding skeletonized images. Flocs and agglomerates lack filament length, leaving blank sections in the third row for these types. Red scale bars in all panels represent 100 μm.

smaller DF2 value indicates that the particle is more compact, while a larger DF2 suggests a more loosely packed structure.

2.6 Processing of water properties data

In this study, the primary seawater properties observed were salinity, turbidity, Chl-a, and particle number concentration throughout the water column. To estimate particle number concentration, we performed vertical averaging at 0.5 m intervals, counting the number of images captured and the total number of particles observed within each section. Given that the sampling volume for each holographic image is V_{holo}, particle number concentration was roughly estimated by dividing the total particle count by the corresponding total volume of captured images. Salinity, turbidity, and Chl-a data were directly obtained from the instruments and averaged to a vertical resolution of 0.5 m per profile. Due to tidal range variations between Stage E and Stage L, water depths differed by 1-2 m; therefore, the depth data were normalized to relative depth (with the sea surface as 0 and the seabed as 1) to facilitate comparison. Additionally, observations from the bottom-mounted platform included turbidity and turbulent kinetic energy dissipation rate. The turbulent kinetic energy dissipation rate (ε) near the bottom boundary layer is calculated using high-frequency fluctuating velocities measured by ADV. The dissipation rate is determined with a temporal resolution of 15 min. This calculation involves transforming the high-frequency vertical fluctuating velocities recorded by the ADV into the vertical turbulence kinetic energy spectrum via Fourier transform. The resulting frequency spectrum is analyzed using Taylor's "frozen field hypothesis" which assumes that turbulence remains steady as it advects past the instrument, without developing or decaying. This assumption allows the conversion of temporal observations into spatial ones (Guerra and Thomson, 2017). Consequently, we obtain the turbulence energy spectrum $E(k)$, which describes the distribution of energy across different wavenumbers k. In the inertial subrange, the energy spectrum adheres to Kolmogorov's theory:

$$E(k) \propto \varepsilon^{2/3} k^{-5/3} \tag{8}$$

The inertial subrange is identified within the wavenumber space where the energy spectrum exhibits a $-5/3$ slope. This identification is typically achieved by examining the log-log plot of the energy spectrum. Once the inertial subrange is determined, a least squares fit is applied to the data within this range to derive the dissipation rate ε (Smith et al., 2005).

3 Results

3.1 Detection results

The training dataset (Section 2.3) comprised a comprehensive and diverse set of particles across seven classes, which were used to train and evaluate the YOLOv5x object detection model (Section 2.4). The training process was configured to run for 150 epochs, with model performance evaluated on the validation set after each epoch. The model that achieved the highest performance metrics during these evaluations was selected as the optimal model. This optimized model was evaluated on a test set of over 2,000 particles, demonstrating robust detection performance by consistently generating accurate bounding boxes, class predictions, and scores in the CFIs (Supplementary Figure 3). The confusion matrix indicated that classification accuracy for all classes exceeded 0.87 (Supplementary Figure 4). Furthermore, the overall mAP0.5 for detected targets reached 0.83, with each individual class achieving an mAP0.5 above 0.70 (detailed results in Supplementary Table 2). The detected targets (seven classes) were primarily divided into two major groups: diatoms, which are living particles and include five classes—diatom beads, diatom chain, diatom coiled, diatom helix, and diatom semicircle; and aggregates, which are mainly formed by biologically mediated flocculation and include two classes—agglomerates and flocs. These classes exhibited significant inter-class variability and intra-class consistency in morphology (Figure 5, more sample images see Supplementary Figure 5). We further categorized the detected targets into Stage E and Stage L, with approximately 6.28×10^4 particles detected in Stage E and 2.09×10^4 particles in Stage L. Diatom particles accounted for 28% and 57% of the total particles in Stage E and Stage L, respectively, while aggregates made up 72% and 43% of the total particles in each stage, respectively. Among the aggregates, flocs were the predominant particle class, constituting 69% of the total particles in Stage E and 33% in Stage L (Supplementary Figure 6).

3.2 Hydrological properties

The hydrodynamic conditions at site S displayed marked differences between Stage E and Stage L. During Stage E, which coincided with the spring tide, the stratified water column was disrupted by the passing typhoon, resulting in a well-mixed state. In contrast, during Stage L, which corresponded with the neap tide, the water column had re-established strong stratification. Tidal cycle-averaged profiles underscored this contrast, showing uniform conditions during Stage E and pronounced stratification during Stage L. Notably, the salinity and temperature differences between the surface and bottom layers were approximately 7 PSU and 2°C during Stage E but increased to 12 PSU and 5°C during Stage L (Figures 7A, B). The turbidity profiles in both stages followed a typical pattern of lower values at the surface and higher values at the bottom, with significant differences between the two stages. In Stage E, strong mixing caused turbidity to increase from 13 NTU at the surface to 28 NTU at the bottom. In Stage L, the variation was less pronounced, with turbidity rising from approximately 7 NTU at the surface to 12 NTU at the bottom. This trend in turbidity mirrored the volume concentration of aggregates, which increased from 3 μL L^{-1} at the surface to 28 μL L^{-1} at the bottom during Stage E, and from 1 to 4 μL L^{-1} during Stage L (Figures 7C, D). The Chl-a concentration profiles also showed higher surface values and lower

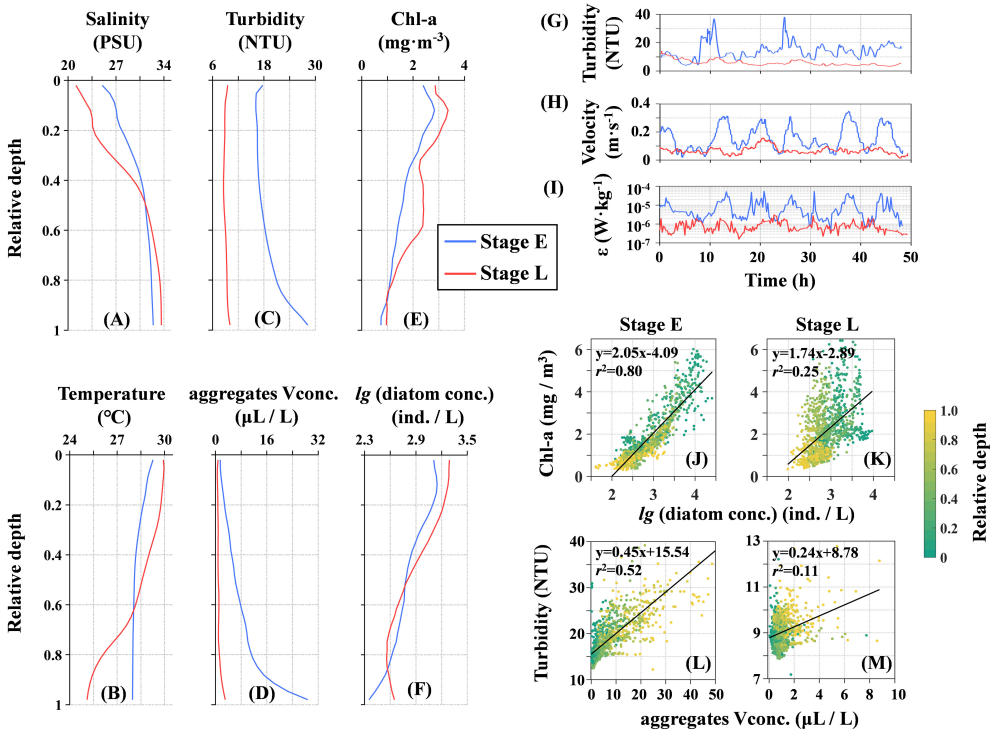

FIGURE 7
Characteristics of seawater properties at site S: Vertically averaged profiles of **(A)** salinity, **(B)** temperature, **(C)** turbidity, **(D)** aggregate volume concentration, **(E)** chlorophyll-a (Chl-a), and **(F)** diatom concentration over the tidal cycle during Stage E (blue) and Stage L (red). Time series of **(G)** turbidity, **(H)** current velocity, and **(I)** turbulent dissipation (ε) near the bottom boundary layer, with the time axis set to relative time starting from zero. Panels **(J, L)** show relationships during Stage E: Chl-a versus diatom number concentration and turbidity versus aggregate volume concentration. Panels **(K, M)** depict these relationships during Stage L. Equations and r^2 values indicate the linear regression models and goodness of fit.

bottom values in both stages, ranging from 1 to 3 mg m^{-3}. Chl-a levels were generally slightly higher in Stage L, with a more pronounced vertical gradient (Figure 7E). The diatom number concentration followed a similar pattern, ranging from $10^{2.3}$ to $10^{3.4}$ individuals L^{-1}, with slightly higher surface values in Stage L and slightly lower bottom values compared to Stage E (Figure 7F). Time series data from the bottom-mounted platform revealed distinct differences in the hydrodynamic structure between the two stages. During Stage E, turbidity ranged from 8 to 35 NTU, whereas in Stage L, it remained consistently below 10 NTU (Figure 7G). The turbulent kinetic energy dissipation rate fluctuated with tidal cycles, closely mirroring the bottom water flow velocity, averaging around 10^{-5} W kg^{-1} in Stage E and 10^{-6} W kg^{-1} in Stage L—approximately an order of magnitude lower (Figures 7H, I). Scatter plot linear regression analyses during Stage E revealed strong positive correlations between Chl-a concentration and diatom number concentration, as well as between turbidity and aggregates volume concentration, with correlation coefficients both exceeding 0.5. In contrast, these relationships were notably weaker during Stage L, with correlation coefficients falling below 0.3 (Figures 7J–M). The implications of this contrast will be explored in greater detail in the Discussion section.

3.3 Particle morphology

A statistical analysis of the morphological parameters of particles across each class during Stage E and Stage L revealed significant inter-class differences among diatom particles, while intra-class variations between the two stages were relatively minor (Figures 8A–C). In Stage L, except for the diatom helix class, which showed an 8% decrease in average FL from approximately 1750 μm to 1600 μm, all other classes exhibited varying degrees of increase. Notably, the average FL in the diatom beads and diatom chain classes increased significantly, by 8% and 27%, from approximately 400 μm and 360 μm to 430 μm and 460 μm, respectively. In contrast, the diatom coiled and diatom semicircle showed smaller increases, with FL rising by about 5% and 4% to approximately 990 μm and 380 μm, respectively (Figure 8A). Regarding changes in the CR, the diatom beads and diatom chain classes exhibited very low curvature, maintaining a straight morphology with average CR values above 0.8. In contrast, diatom coiled and diatom helix had average CR values below 0.4, while diatom semicircle had an average CR of around 0.6. Apart from diatom coiled, which showed a slight increase in both FL and CR during Stage L compared to Stage E, the other diatom classes exhibited an increase in FL alongside a corresponding decrease in CR during

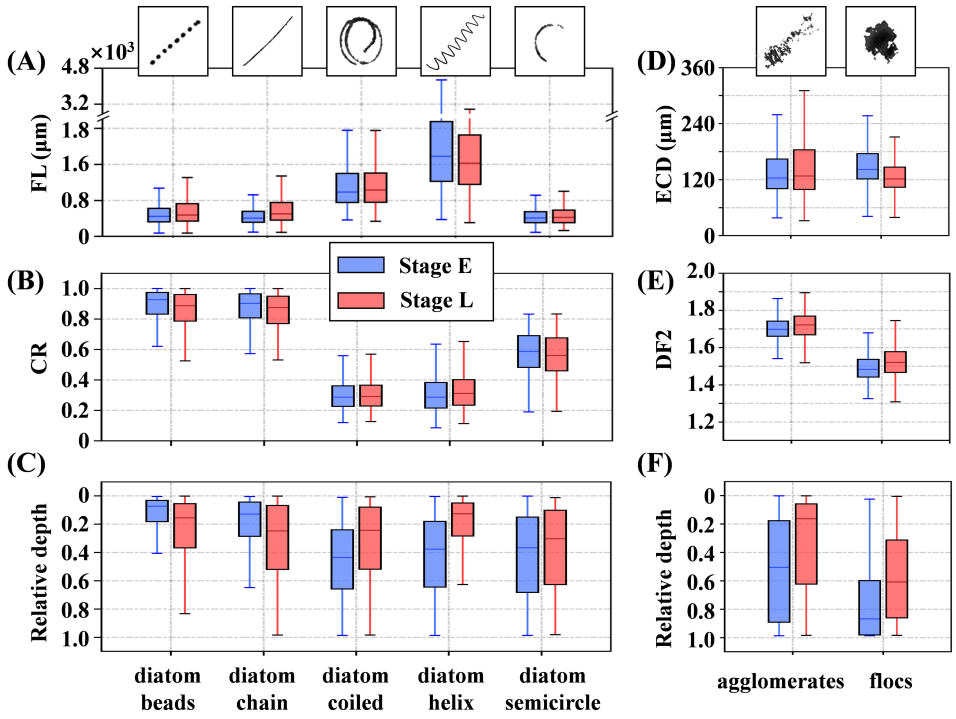

FIGURE 8
Particle morphological parameters of different classes during Stage E (blue) and Stage L (red) are shown. The left column represents diatom particles, detailing: **(A)** filament length (FL), **(B)** coiling ratio (CR), and **(C)** distribution at relative depth (surface = 0, bottom = 1). The right column depicts aggregates, illustrating: **(D)** equivalent circular diameter (ECD), **(E)** perimeter-based two-dimensional fractal dimension (DF2), and **(F)** distribution at relative depth. The heights of the box plots indicate the interquartile range (25th to 75th percentile), the lines within the boxes represent the median (50th percentile), and the whiskers extend to the maximum and minimum values within 1.5 times the interquartile range, without exceeding the actual data range.

Stage L (Figure 8B). These results suggest that FL and CR generally follow an inverse trend, where diatoms with longer FL tend to have lower CR, indicating a higher degree of curvature (Supplementary Figures 7A, B). In both stages, diatoms were primarily concentrated in the upper half of the water column above 0.5 H.

The elongated-curled diatoms, such as diatom coiled and diatom helix, exhibited a deeper and broader average distribution depth during Stage E compared to Stage L. Conversely, the short-straight diatoms, including diatom beads and diatom chain, were more concentrated in the surface layer during Stage E than in Stage L (Figure 8C). Notably, regardless of the stage, the FL of diatom semicircle was comparable to that of diatom beads and diatom chain, but its average distribution depth was both deeper and more extensive than those of the latter two. The differences between the agglomerates and flocs became more pronounced between Stage E and Stage L. The ECD of agglomerates increased slightly by 3%, from 124 μm in Stage E to 128 μm in Stage L, while their average DF2 increased from 1.70 to 1.72, indicating that agglomerates became more loosely packed. In contrast, flocs exhibited more significant changes, with their average ECD decreasing by 14% from 142 μm to 122 μm, while their average DF2 increased from 1.48 to 1.52. During Stage E, agglomerates were distributed throughout much of the water column, but in Stage L, they became concentrated primarily in the upper layer above 0.6 H. Flocs, on the other hand, were mainly concentrated near the bottom. They were more confined to areas below 0.6 H during Stage E, while in Stage L, their distribution expanded, concentrating primarily below 0.3 H. The relationship between ECD and DF2 in these aggregates did not show a clear correlation. Aggregates with ECDs near the average value could exhibit either a high DF2, indicating a loose structure, or a low DF2, indicating a compact structure (Supplementary Figures 7C, D).

3.4 Particle vertical distribution

The number concentration and distribution of diatoms and aggregates at site S exhibited significant differences between Stage E and Stage L. Diatoms were primarily concentrated in the upper half of the water column, with short-straight diatoms (e.g., diatom beads and diatom chain) showing the highest concentrations. Although their number concentration slightly decreased from Stage E to Stage L, both stages consistently revealed higher concentrations of these diatoms near the surface (Figures 9B, C). In contrast, the elongated-curled diatoms (e.g., diatom coiled, diatom helix, and diatom semicircle) showed a slight increase in maximum concentrations from Stage E to Stage L, with a deeper and broader distribution range during Stage E compared to Stage L (Figures 9D–F). For aggregates, flocs had significantly higher concentrations than agglomerates. Agglomerates were more concentrated in the mid-to-upper layers, with Stage E showing lower surface concentrations than Stage L. However, the vertical distribution of agglomerates

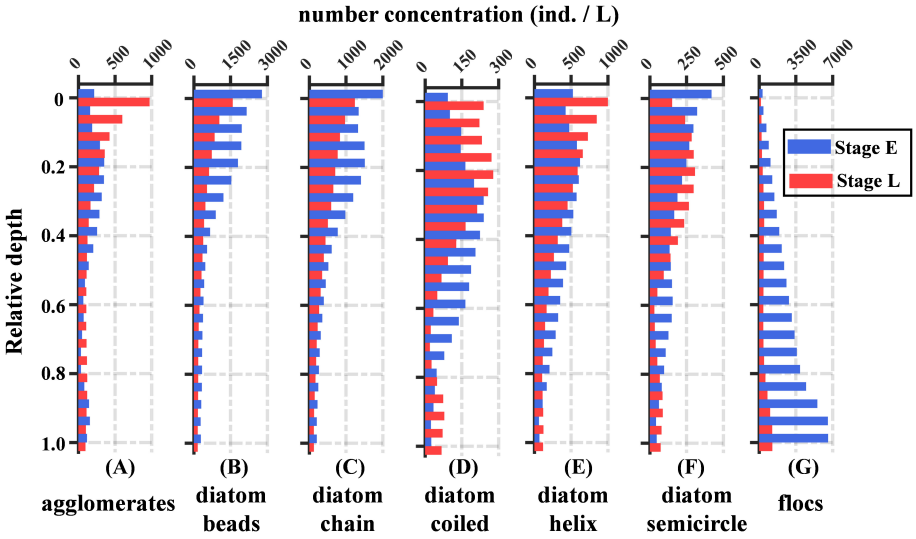

FIGURE 9
The average vertical profiles of particle number concentration for each class over two tidal cycles are presented for Stage E (blue bars) and Stage L (red bars). The classification from **(A–G)** represents agglomerates, diatom beads, diatom chain, diatom coiled, diatom helix, diatom semicircle, and flocs.

during Stage E was more uniform compared to Stage L (Figure 9A). The concentration of flocs increased from the surface to the bottom in both stages, but concentrations below 0.5 H were notably higher during Stage E than in Stage L (Figure 9G).

To investigate the depth-dependent distribution of particle morphology, we classified all detected particles into two main groups: diatoms and aggregates, analyzing their respective parameters—FL and CR for diatoms, and ECD and DF2 for aggregates. The water column was divided into ten layers based on relative depth, with one-dimensional kernel density estimation applied to each parameter within these layers (Figure 10). In Stage E, diatoms exhibited an increase in median FL with depth, along with a more dispersed distribution. Conversely, in Stage L, the median FL slightly decreased with depth, becoming more concentrated. The median CR displayed a similar downward trend with depth in both stages. At the surface, two peaks in CR

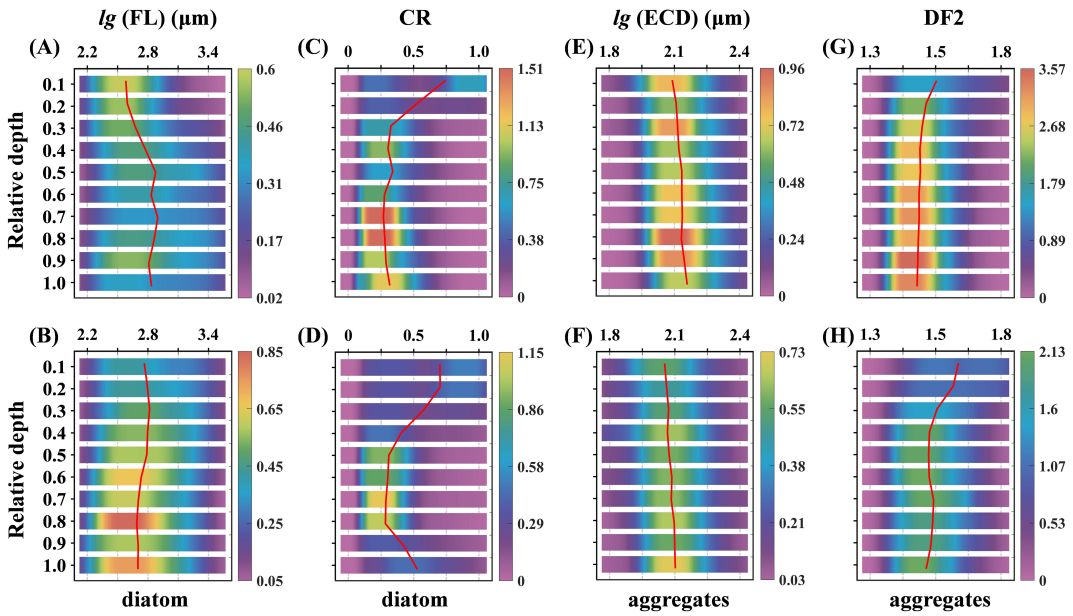

FIGURE 10
Depth-resolved kernel density estimate plots for Stage E **(A, C, E, G)** and Stage L **(B, D, F, H)** are shown, with relative depth from surface (0) to bottom (1) divided into ten segments to depict particle distribution. Each segment has a heatmap representing the kernel density estimation of the parameter using a Gaussian kernel, indicating parameter density within this space. Red curves represent the median parameter distribution (cumulative density of 0.5) at each depth segment.

values were observed, indicating a diverse population of diatoms, with both straight and coiled forms prominent. As depth increased, the CR distribution became more concentrated, dominated by lower CR values, indicative of more coiled diatoms. For aggregates, the median ECD increased with depth during both stages, while the median DF2 decreased. Notably, during Stage E, the median ECD values were larger and the median DF2 values smaller across all layers compared to Stage L, suggesting that aggregates formed during Stage E were generally larger and more compact throughout the water column.

To investigate how morphological parameters influence the distribution of diatoms and aggregates within the water column, we first applied two-dimensional kernel density estimation to analyze FL and relative depths. This analysis enabled the classification of diatoms into two distinct groups based on their CR: those with a CR< 0.7, which correspond to elongated-curled diatoms, and those with a CR > 0.7, representing short-straight diatoms (Figures 8A, B). The elongated-curled diatoms, characterized by longer median FL ranging from approximately $10^{2.5}$ to $10^{3.7}$ µm, exhibited significant vertical distribution variations that correlated with changes in water structure. During the well-mixed conditions of Stage E, these diatoms settled deeper, reaching depths around 0.8 H (Figure 11A). However, in the strongly stratified conditions of Stage L, their settlement was restricted to shallower depths around 0.4 H (Figure 11B). In contrast, the short-straight diatoms, with shorter median FL ranging from $10^{2.0}$ to $10^{3.4}$ µm, were less influenced by water conditions and consistently concentrated in the upper 0.2 H of the water column across both stages (Figures 11C, D).

Similarly, aggregates were analyzed using kernel density estimation based on their ECD and relative depths. They were categorized into two types based on their DF2 values: compact aggregates (DF2< 1.6) and loose aggregates (DF2 > 1.6) (Figures 8D, E). Compact aggregates, with median ECD ranging from approximately $10^{1.5}$ to $10^{2.5}$ µm, were predominantly concentrated near the seabed during Stage E, with their concentration increasing with depth. Despite a significant decrease in compact aggregates during Stage L, they remained primarily near the seabed, exhibiting a more uniform vertical distribution and a noticeable presence even in the upper layers (Figures 11E, F). On the other hand, loose aggregates, characterized by median ECD ranging from $10^{1.5}$ to $10^{2.7}$ µm, displayed distinctly different distribution patterns between the stages. In Stage E, they were mainly concentrated near the bottom but were more evenly distributed throughout the water column, including the middle and upper layers. In Stage L, loose aggregates were primarily found near the surface, with some high-concentration areas near the bottom, while the middle layers exhibited lower concentrations (Figures 11G, H).

4 Discussion

4.1 Holographic images provide more accurate information

This study introduces an innovative algorithm for efficiently generating large sets of CFIs that capture essential particle shapes and textures (Figure 5). Compared to Sequoia's HOLO batch software, our method significantly improves target recognizability, as demonstrated by images and parameter calculations in Supplementary Figure 9. Despite being grayscale, these CFIs retain critical morphological details, enabling high performance in object detection models while reducing computational costs by using only one-third the data volume of color images (Bui et al., 2016),

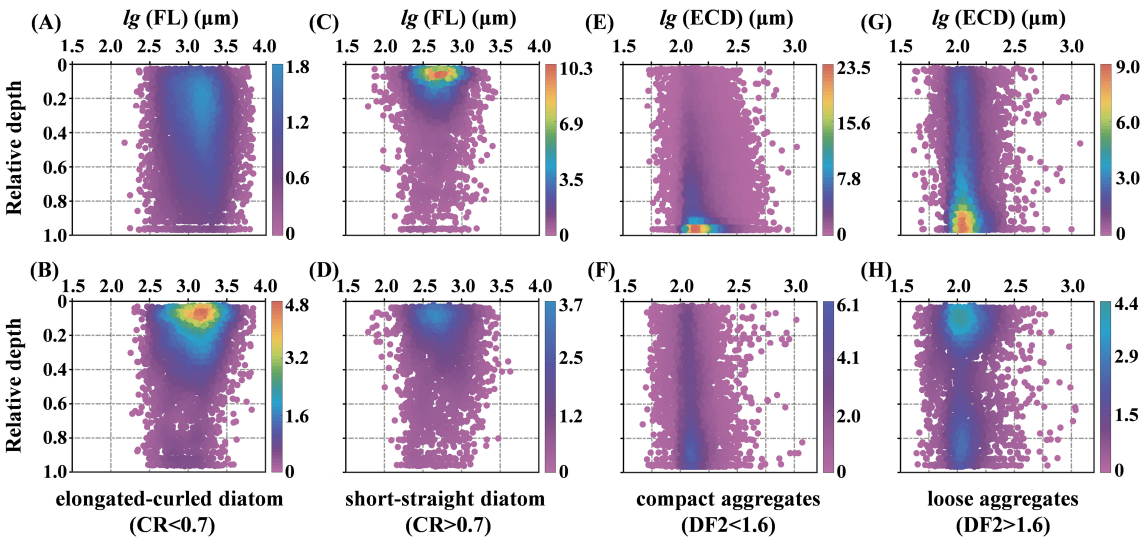

FIGURE 11
2D kernel density plots of particle morphological parameters and relative depth. These figures illustrate the relationships between various parameters and their corresponding relative depths, ranging from the surface (0) to the bottom (1). The panels **(A, C, E, G)** correspond to Stage E, and the panels **(B, D, F, H)** correspond to Stage L. Each point represents an individual detected particle, with coordinates determined by its properties. The color represents Gaussian kernel density estimation, indicating particle distribution density, with color bars on the right showing the density scale.

underscoring the practical benefits of our holographic image processing approach. Furthermore, the object detection model accurately defines bounding boxes around targets, which is crucial for extracting morphological parameters from cropped particle images. Direct binarization of CFIs often causes fragmentation, especially in particles with transparent or thin connections like diatom beads, leading to scattered fragments (Figure 6A). This fragmentation varies by binarization method, affecting flux and concentration estimates (Giering et al., 2020). Object detection models mitigate this by bounding entire targets, ensuring fragments are recognized as a single object, reducing errors in calculating parameters like filament length and making them reliable for CFI analysis.

Utilizing the object detection model enhances particle classification and extraction in CFIs, enabling more accurate concentration measurements (Figure 9). This approach offers greater efficiency and precision compared to traditional water sampling and microscopy (Lund et al., 1958). While conventional methods infer algal concentration indirectly through Chl-a, our holographic imaging findings show that diatom and Chl-a concentrations do not consistently correlate across depths and time intervals (Figures 7J, K). During Stage E, a strong linear relationship indicates that Chl-a can reflect diatom concentration under certain conditions (Figure 7J), but this weakens in Stage L due to diatom degradation (Figure 7K). This spatial and temporal decoupling (Supplementary Figures 8A, B, E, F) highlights the limitations of relying solely on Chl-a to infer diatom concentration. Furthermore, previous studies have raised concerns about the accuracy of using chlorophyll fluorescence as a proxy for Chl-a (Cullen, 1982), reinforcing the need for direct observational data and experimental validation (Cullen, 2015). In this context, holographic imaging not only provides valuable data for correlating Chl-a with diatom biomass but also offers direct, visual measurements of algal concentration, making it a more reliable alternative.

Similarly, traditional methods often estimate the volume or mass concentration of suspended particles based on turbidity (Bunt et al., 1999). However, our results show that estimating aggregate volume concentration based on ECD from detected images does not consistently produce a strong linear correlation with turbidity. While the relationship between aggregate volume concentration and turbidity is similar to that of diatoms, it is not always linear. In Stage E, aggregates dominate particle concentration and strongly correlate with turbidity (Figure 7L); however this correlation weakens considerably in Stage L (Figure 7M), likely due to stratification, which reduces aggregates below the pycnocline. Simultaneously, shear at the pycnocline can cause elongated diatoms to rotate and align with the shear flow, enhancing photosynthetic efficiency (Nayak et al., 2018) and potentially increasing optical backscattering by up to 35% (Marcos et al., 2011). These findings indicate that relying solely on turbidity to measure volume or mass concentration without considering particle composition can yield inaccurate results. The coexistence of diatoms and aggregates, with their distinct morphologies, further complicates turbidity measurements. Studies have also shown that this affects size measurements using laser scattering methods like LISST, potentially misinterpreting sub-scales as independent particles (Graham et al., 2012). In contrast, holographic imaging, with its particle classification capabilities, provides detailed distribution data (Figure 10), enabling more accurate interpretations of turbidity and LISST measurements.

4.2 Ecological insights from particle morphology in holographic images

Statistical analysis of FL and DF2 for all diatoms reveals that morphological variation in diatoms is not continuous but primarily falls into two major categories: short-straight and elongated-curled forms (Supplementary Figures 7A, B). Straight diatoms generally exhibit shorter FL (Figure 8), with variations in cell connectivity leading to distinct classes in CFIs, as diatom beads and diatom chain. For example, in species like *Thalassiosira*, synthesized chitin threads between cells (Gherardi et al., 2016), though not fully visible in CFIs, result in a bead-string appearance (Figure 5B). Similar patterns are observed in *Skeletonema* (Figure 4B), while other short-straight diatoms, such as *Aulacoseira* (Figure 4C) and *Pseudo-nitzschia* (Figure 4D), appear as solid lines (Figure 5C). Despite differences in cell connectivity, these diatoms maintain a unified short-straight morphology in CFIs. Experimental studies suggest that short-straight diatoms, such as *Skeletonema* typically exhibit minimal curvature and strong rigidity, which enhance their resistance to shear forces (Young et al., 2012) and nutrient uptake (Musielak et al., 2009). In contrast, curled diatoms with longer FL display varying degrees of curvature, forming diatom coiled, diatom helix, and diatom semicircle classes. The genus *Chaetoceros*, which connects via frustule processes (Fryxell, 1978), exemplifies this, with species like *Chaetoceros pseudocurvisetus* (Figures 4E, G) classified as diatom coiled and diatom semicircle, and *Chaetoceros debilis* (Figure 4F) as diatom helix. However, this morphological diversity among diatoms complicates their precise classification based solely on CFIs. Research indicates that longer, flexible diatoms maintain chain integrity in turbulent waters, resisting breakage under mechanical stress (Karp-Boss and Jumars, 1998). Additionally, flexible chains may also have higher "morphological stickiness" increasing their likelihood of entanglement and cohesion, which facilitates aggregation.

Beyond species identification, these morphological parameters provide valuable insights into environmental and ecological shifts. Diatom morphological traits, such as size and shape, respond to environmental conditions and reflect their ecological functions and adaptability (Naselli-Flores et al., 2007). FL and CR, as key morphological functional traits, can serve as indicators of environmental changes. Additionally, the mechanical properties of diatoms, including flexibility and rigidity, influence their interactions with the physical environment. The comprehensive *in situ* data provided by CFIs allows for detailed analysis of algal vertical distribution, facilitating deductions regarding environmental impacts on diatom communities. Studies have also shown that diatoms produce transparent exopolymer particles (TEP), a gelatinous substance that plays a crucial role in aggregating suspended sediments into large organic aggregates

(Passow, 2002). This process is particularly significant in coastal areas with high resuspension, where the resulting aggregates display diverse morphologies and smooth transitions between types (Figure 5G). The morphological traits of these aggregates can reflect the intensity of diatom activity. By analyzing the ECD and DF2 of aggregates, we can use these key indicators of size and density to assess environmental changes, including biologically mediated flocculation and turbulent shear (Maggi, 2007). In the following section, we will explore particle dynamics using these morphological traits to examine hydrodynamic changes in the estuarine environment from an *in situ* perspective.

4.3 Suspended particles dynamics during the typhoon-induced algal blooms

During Stage E, the well-mixed state driven by tidal stirring at the seabed produced turbulence with kinetic energy dissipation an order of magnitude higher than in Stage L (Figure 7I). This enhanced turbulence propagated throughout the entire water column (Coogan et al., 2020), intensifying sediment resuspension and promoting the downward diffusion of surface diatom particles (Figure 12A; time-series data in Supplementary Figure 8). The increase in suspended sediments, combined with enhanced turbulence, led to frequent particle collisions, forming larger, denser flocs (Burd and Jackson, 2009). Physically, in these highly mixed, non-stratified conditions, surface phytoplankton layers were dissipated by turbulence (Stacey et al., 2007). Our observations showed that the downward diffusion of diatoms follows a distinct tidal cycle (Supplementary Figures 8A, B), suggesting that strong mixing prevents the formation of a stable surface phytoplankton layer. This underscores the crucial role of tidal mixing in driving the downward transport and distribution of diatoms, particularly affecting elongated-curled forms. While laboratory studies suggest that elongating diatom chains increases settling resistance and reduces settling velocity (Takabayashi et al., 2006); our results show that elongated-curled diatoms with larger FL settled at greater depths, indicating that physical mixing dominates their passive settling rather than active regulation. Statistical analysis also revealed that diatoms with greater curvature (lower CR values) had a diffusion advantage even when FL was similar, as seen in the comparison between diatom chains and semicircles (Figure 9C). This aligns with Padisak (2003) experiment using a physical model of diatoms, which found that greater curvature reduces settling resistance, reinforcing that elongated-curled diatoms are more prone to settling in mid to deeper layers. These findings highlight the differentiation of morphological traits in diatom distribution within strongly mixed environments. Biogeochemically, strong mixing increased nutrient availability throughout the water column, accelerating diatom proliferation. Enhanced turbulence promotes nutrient uptake by reducing the thickness of the boundary layer around diatoms, increasing nutrient flux and stimulating growth (Prairie et al., 2012). However, diatom species and morphologies respond differently to turbulence. For example, *Chaetoceros*, with its elongated, flexible chains, increased net carbon assimilation by 59%, while *Skeletonema*, with shorter, rigid chains, showed a 31% increase (Bergkvist et al., 2018). Under nutrient-rich conditions, diatoms excrete part of the fixed carbon as transparent exopolymer particles (TEP), which promote the flocculation of suspended sediments. Flocs formed from suspended sediments alone are typically small, but TEP from chain-forming diatoms can result in much larger flocs (Hamm, 2002). Our observations confirmed this, with many aggregates exceeding the Kolmogorov microscale of turbulence (Supplementary Figure 10). The abundance of elongated-curled diatoms and their higher carbon assimilation rates in the middle and bottom layers during Stage E likely contributed to the formation of larger, denser flocs compared to Stage L (Figures 10E–H). Strong turbulence facilitated the settling of these diatoms, forming numerous loose algal agglomerates. The high concentration of suspended sediment may attach to these agglomerates (Supplementary Figure 11) further increased their density and settling velocity, explaining why large agglomerates were primarily found in the middle and bottom layers during Stage E (Figure 11G).

During Stage L, strong stratification reestablished, as shown by significant salinity and temperature gradients (Figures 7A, B) and particle distribution patterns (Figure 12B; time-series data in Supplementary Figure 8). Physically, this stratification inhibited turbulent diffusion from tidal stirring, leading to reduced turbulent dissipation and sediment resuspension (Figures 7G, I) (Coogan et al., 2020). As turbulence decreased, suspended sediment concentration and collision frequency dropped, resulting in smaller floc sizes. This stratified structure caused diatoms to distribute unevenly throughout the water column, forming a surface phytoplankton thin layer in the upper 0.4 H. Such layers typically develop in stable waters with minimal tidal mixing (Prairie et al., 2012). FL of diatoms generally increased during Stage L, especially in short-straight diatoms like the diatom chain class, which grew by 27% (Figure 8A), likely due to reduced turbulence minimizing mechanical disruption. Biogeochemically, stratification restricted the vertical supply of nutrients (Barton et al., 2013), exacerbating nutrient depletion in the upper layers. As the algal bloom entered its late phase, diatoms faced intensified competition and increased mortality. Our observations of increased FL suggest that under nutrient-limited conditions, diatoms may switch from asexual to sexual reproduction, further contributing to longer FL (Litchman and Klausmeier, 2008). Consequently, diatom morphology and life processes played a critical role in determining their distribution within the surface phytoplankton layer. Bergkvist et al. (2018) demonstrated that under nutrient-limited conditions, *Chaetoceros*, with longer filaments, grew faster than the shorter-straight *Skeletonema*, a pattern also reflected in our observations. During Stage L, a slight reduction in the concentration of short-straight diatoms was noted (Figures 8B, C), indicating a decline in their competitiveness. In contrast, elongated-curled diatoms showed a broader distribution, extending toward the lower boundary of the thin layer (Figure 11B), while short-straight diatoms remained concentrated in the upper part (Figure 11D). This suggests that elongated-curled diatoms, with greater activity, are better adapted to inhabiting deeper layers. These differential growth dynamics likely contributed to the observed distribution patterns within the thin layer. As in Stage E, the distribution of algal agglomerates was closely tied to that of diatoms, particularly elongated-curled forms, leading to agglomerates concentrating near the surface (Figure 11H). In the late bloom stages, the decomposition of surface diatoms released large amounts of Chl-a and TEP, which diffused into deeper layers,

weakening the correlation between diatom and Chl-a concentrations (Figure 7K). Although sediment resuspension decreased significantly, excess TEP and biogenically mediated flocculation persisted, resulting in flocs that remained larger than those flocculated from pure mineral clay particles. Thus, the weakened turbulence in Stage L was the primary factor leading to the formation of smaller and less dense flocs compared to Stage E, and allowed low-density flocs and agglomerates to distribute more evenly across the vertical profile in the stratified water column (Figures 11F, H).

4.4 Ecological implications in estuarine systems

The findings indicate that changes in particle morphology and distribution in shallow estuaries are far more complex due to physical dynamics. During Stage E, strong mixing can drive elongated-curled diatoms into deeper layers. Although this reduces their sunlight exposure, intense turbulence enables them to sustain high rates of nutrient uptake and carbon assimilation. This photosynthetic activity contributes to replenishing dissolved oxygen and offers a potential explanation for the mechanisms underlying the impact of typhoons on estuarine hypoxia. Furthermore, this process enhances the incorporation of organic carbon into denser, biologically-mediated flocs, intensifying the carbon pump and increasing organic carbon deposition on the estuary floor. The subsequent bacterial respiration and decomposition of these materials may contribute to the worsening hypoxia observed after typhoons (Wang et al., 2017). The restoration of stratification triggers morphological and distributional changes in diatoms within surface phytoplankton layers. Traits such as FL elongation and the spread of elongated-curled forms become more pronounced. Understanding these changes is crucial for interpreting how external physical variations and diatom life cycles evolve during algal bloom development. These findings suggest that diatom morphology, rather than species-specific differences, is more responsive to environmental factors, reinforcing the idea that coastal ecosystem functions are shaped by the functional traits of organisms rather than their taxonomic composition (Martini et al., 2021).

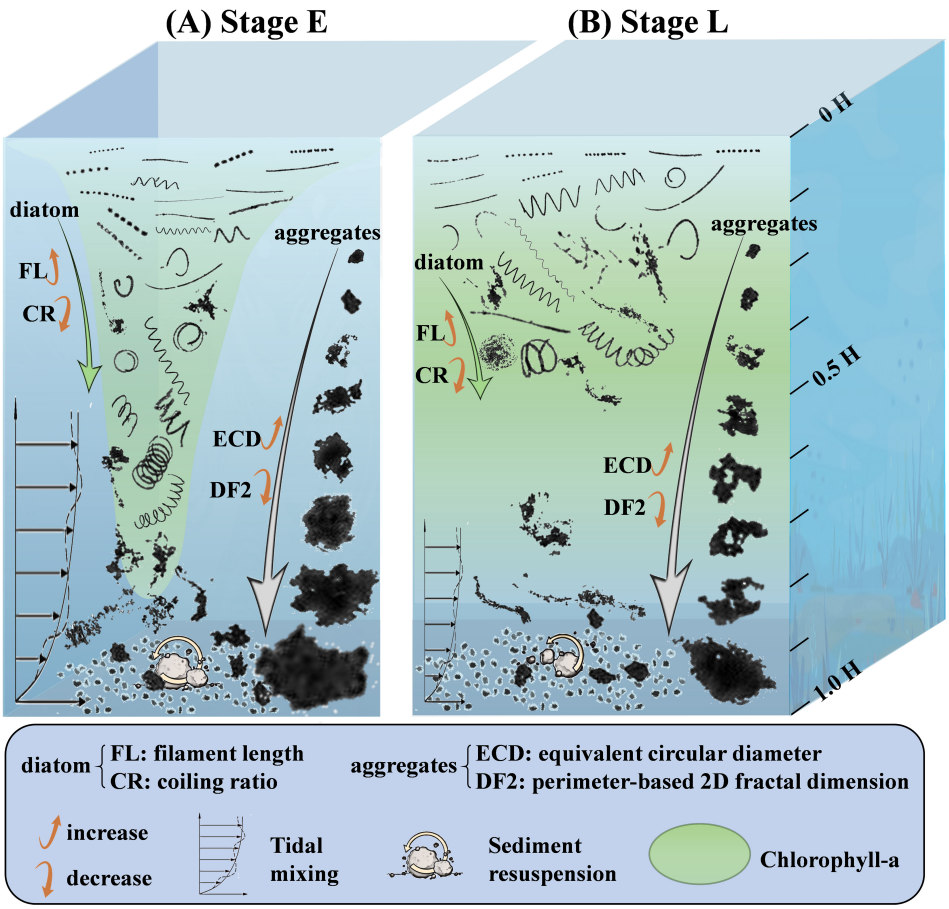

FIGURE 12
A conceptual diagram illustrates the particle distribution during the **(A)** early stage (Stage E) and **(B)** late stage (Stage L) of the typhoon-induced algal bloom. In both stages, diatom FL increases, and CR decreases with depth. For flocs, ECD increases while DF2 decreases with increasing depth. During Stage E, enhanced turbulent mixing facilitates the settling and downward extension of diatoms, driven by tidal mixing. At this stage, the mean ECD and density of flocs are greater, with higher concentrations compared to Stage L. In Stage L, strong stratification of the water column leads to the formation of diatom layers near the surface, with Chl-a diffusion extending beyond the diatom distribution range. These variations in particle morphology and distribution reflect the distinct characteristics of each developmental stage of the typhoon-induced algal bloom.

Similarly, aggregate morphology and distribution provide valuable insights into environmental changes that traditional particle size distribution analyses, such as laser diffraction, may not fully capture. As aggregate morphology is strongly influenced by turbulence intensity and algae-aggregate interactions, understanding these factors requires more than conventional methods. In our research, analyzing image-derived parameters provides foundational data for calculating key metrics. When integrated with empirical studies, these metrics can further advance the assessment of parameters such as three-dimensional fractal dimension (Tang and Maggi, 2015), particulate organic carbon influx (Durkin et al., 2021), and settling velocity (Many et al., 2019). This approach holds potential to uncover broader relationships between particles and ecological processes, including trophic interactions, carbon cycling, and nitrogen cycling.

In this study, FL and CR were identified as cross-taxon traits applicable across species, while ECD and DF2 demonstrated measurable responses of aggregate morphology to environmental changes. These traits offer an efficient and valuable approach to analyzing estuarine ecosystems and algal bloom evolution. Since functional traits transcend species classifications, they help mitigate the negative impacts of taxonomic inconsistencies in diatom data (Riato et al., 2022). Extracting these morphological parameters from images offers a more convenient and cost-effective alternative to genetic sequencing. Despite these advances, the extraction and quantification of particle functional traits remain underexplored (Trudnowska et al., 2021). The scarcity and diversity of particle images present challenges in building comprehensive relationships between particle morphology and environmental interactions from large datasets. Future research will require more advanced image detection techniques and morphology extraction models. The methods and findings from this study provide valuable references for future research into aquatic particle morphology. As *in situ* imaging technology and artificial intelligence continue to advance, expanding the collection of particle image data is crucial, as the wealth of information embedded in particle morphology remains largely untapped. Research on particle functional traits suggests that using a few key variables to predict environmental changes holds significant potential.

5 Conclusion

When a typhoon disrupts the stratified structure of coastal waters, it generates a mixed water column. This column, driven by tidal forces and runoff, creates a complex hydrodynamic environment profoundly influences the distribution and behavior of suspended particles. Analyzing and detecting these particles under such dynamic conditions using high-resolution *in situ* data is essential for understanding the evolution of estuarine ecosystems. In this study, two consecutive mooring observations were conducted in the PRE following Typhoon Cempaka in 2021, capturing holographic images of particles and collecting hydrological data during different stages of an algal bloom. Based on these data, we developed an effective algorithm to process the holographic images, generating CFIs with clear target contours, that are ideal for building datasets for object detection models. Using a trained object detection model, we efficiently collected and analyzed various particle classes and morphological traits. Statistical analysis of these data demonstrates that holographic imaging provides more precise hydrological data than traditional methods, including particle morphology, concentration, classification, and vertical distribution.

The study revealed that elongated-curled diatoms tend to settle into mid-bottom layers under strong mixing conditions but concentrate in the surface phytoplankton layer in stratified waters. In contrast, short-straight diatoms exhibit minimal sensitivity to physical dynamics and remain concentrated near the surface. Loose aggregates, primarily composed of algal agglomerates, are closely associated with elongated-curled diatoms, distributing in both the surface and bottom layers under strong mixing but concentrating in the surface layer in stratified waters. Compact aggregates, mainly composed of flocs, are primarily distributed near the bottom, with their concentration linked to sediment resuspension caused by turbulence. Their size and density are influenced by biologically mediated flocculation processes related to diatom concentration. The study also found an increase in overall filament length of diatoms, with the concentration of elongated-curled diatoms rising while that of short-straight diatoms declined. These functional trait changes reflect diatom life cycles at various stages of algal bloom development. The decrease in floc concentration, along with the reduction in particle size and density, mirrors the fluctuating strength of external physical forces and shifts in diatom concentration. These findings suggest that the *in situ* functional traits of particles can serve as indicators of environmental changes in estuarine ecosystems, with the *in situ* statistical results providing valuable validation references for water sample analysis and laboratory research. These functional traits hold considerable ecological research value. Moving forward, the full potential of intelligent holographic technology in *in situ* particle detection should be harnessed to enhance data collection and build a more comprehensive classification and statistical database for suspended particles.

Data availability statement

The original contributions presented in the study are included in the article/Supplementary Material. Further inquiries can be directed to the corresponding author.

Author contributions

YL: Data curation, Formal analysis, Methodology, Writing – original draft. LY: Data curation, Formal analysis, Funding acquisition, Writing – original draft. CL: Data curation,

Investigation, Writing – original draft. YC: Data curation, Investigation, Writing – original draft. JW: Conceptualization, Funding acquisition, Supervision, Writing – review & editing.

Funding

The author(s) declare financial support was received for the research, authorship, and/or publication of this article. This study was supported by the National Natural Science Foundation of China (Grant No. 42161160305, 42106160, 12411530095, 42476155, 42076173) and National Science Foundation of China-Guangdong Joint Funding (Grant No. U1901209).

Acknowledgments

We greatly appreciate Mr. Zhenkun Lin, Keyan Liu, Zhe Zhang and Jinglun Huang for their helps in the *in situ* survey. We also thank the captain and crews of R/V Haike 68 for their cooperation during the field observations.

Conflict of interest

The authors declare that the research was conducted in the absence of any commercial or financial relationships that could be construed as a potential conflict of interest.

Publisher's note

Supplementary material

The Supplementary Material for this article can be found online at: https://www.frontiersin.org/articles/10.3389/fmars.2024.1499002/full#supplementary-material

References

Amato, A., Dell'Aquila, G., Musacchia, F., Annunziata, R., Ugarte, A., Maillet, N., et al. (2017). Marine diatoms change their gene expression profile when exposed to microscale turbulence under nutrient replete conditions. *Sci. Rep.* 7, 3826. doi: 10.1038/s41598-017-03741-6

Barton, A. D., Pershing, A. J., Litchman, E., Record, N. R., Edwards, K. F., Finkel, Z. V., et al. (2013). The biogeography of marine plankton traits. *Ecol. Lett.* 16, 522–534. doi: 10.1111/ele.12063

Bergkvist, J., Klawonn, I., Whitehouse, M. J., Lavik, G., Brüchert, V., and Ploug, H. (2018). Turbulence simultaneously stimulates small- and large-scale CO2 sequestration by chain-forming diatoms in the sea. *Nat. Commun.* 9, 3046. doi: 10.1038/s41467-018-05149-w

Boyd, P. W., Claustre, H., Levy, M., Siegel, D. A., and Weber, T. (2019). Multi-faceted particle pumps drive carbon sequestration in the ocean. *Nature* 568, 327–335. doi: 10.1038/s41586-019-1098-2

Briggs, N., Dall'Olmo, G., and Claustre, H. (2020). Major role of particle fragmentation in regulating biological sequestration of CO2 by the oceans. *Science* 367, 791–793. doi: 10.1126/science.aay1790

Bui, H. M., Lech, M., Cheng, E., Neville, K., and Burnett, I. S. (2016). "Using grayscale images for object recognition with convolutional-recursive neural network," in *2016 IEEE Sixth International Conference on Communications and Electronics (ICCE)*, Ha-Long City, Quang Ninh Province, Vietnam., 321–325. doi: 10.1109/CCE.2016.7562656

Bunt, J. A. C., Larcombe, P., and Jago, C. F. (1999). Quantifying the response of optical backscatter devices and transmissometers to variations in suspended particulate matter. *Cont. Shelf Res.* 19, 1199–1220. doi: 10.1016/S0278-4343(99)00018-7

Burd, A. B., and Jackson, G. A. (2009). Particle aggregation. *Annu. Rev. Mar. Sci.* 1, 65–90. doi: 10.1146/annurev.marine.010908.163904

Chavez, F. P., Messié, M., and Pennington, J. T. (2011). Marine primary production in relation to climate variability and change. *Annu. Rev. Mar. Sci.* 3, 227–260. doi: 10.1146/annurev.marine.010908.163917

Choi, S. M., Seo, J. Y., Lee, G., Shen, X., and Ha, H. K. (2021). Practical method to screen contaminated holograms of flocs using light intensity. *Front. Mar. Sci.* 8. doi: 10.3389/fmars.2021.695510

Coogan, J., Dzwonkowski, B., Park, K., and Webb, B. (2020). Observations of restratification after a wind mixing event in a shallow highly stratified estuary. *Estuaries Coasts.* 43, 272–285. doi: 10.1007/s12237-019-00689-w

Cullen, J. J. (1982). The deep chlorophyll maximum: comparing vertical profiles of chlorophyll a. *Can. J. Fish. Aquat. Sci.* 39, 791–803. doi: 10.1139/f82-108

Cullen, J. J. (2015). Subsurface chlorophyll maximum layers: enduring enigma or mystery solved? *Annu. Rev. Mar. Sci.* 7, 207–239. doi: 10.1146/annurev-marine-010213-135111

Dai, Y., Yang, S., Zhao, D., Hu, C., Xu, W., Anderson, D. M., et al. (2023). Coastal phytoplankton blooms expand and intensify in the 21st century. *Nature* 615, 280–284. doi: 10.1038/s41586-023-05760-y

De Nicola, S., Finizio, A., Pierattini, G., Ferraro, P., and Alfieri, D. (2005). Angular spectrum method with correction of anamorphism for numerical reconstruction of digital holograms on tilted planes. *Opt. Express* 13, 9935–9940. doi: 10.1364/OPEX.13.009935

Diplaros, A., Vlassis, N., and Gevers, T. (2007). A spatially constrained generative model and an EM algorithm for image segmentation. *IEEE Trans. Neural Netw.* 18, 798–808. doi: 10.1109/TNN.2007.891190

Durkin, C. A., Buesseler, K. O., Cetinić, I., Estapa, M. L., Kelly, R. P., and Omand, M. (2021). A visual tour of carbon export by sinking particles. *Global Biogeochem. Cycles* 35, e2021GB006985. doi: 10.1029/2021GB006985

Fryxell, G. A. (1978). Chain forming diatoms: three species of Chaetoceraceae. *J. Phycol.* 14, 62–71. doi: 10.1111/j.1529-8817.1978.tb00633.x

Gherardi, M., Amato, A., Bouly, J.-P., Cheminant, S., Ferrante, M. I., d'Alcalá, M. R., et al. (2016). Regulation of chain length in two diatoms as a growth-fragmentation process. *Phys. Rev. E* 94, 22418. doi: 10.1103/PhysRevE.94.022418

Giering, S. L. C., Hosking, B., Briggs, N., and Iversen, M. H. (2020). The interpretation of particle size, shape, and carbon flux of marine particle images is strongly affected by the choice of particle detection algorithm. *Front. Mar. Sci.* 7. doi: 10.3389/fmars.2020.00564

Graham, G. W., Davies, E. J., Nimmo-Smith, W. A. M., Bowers, D. G., and Braithwaite, K. M. (2012). Interpreting LISST-100X measurements of particles with complex shape using digital in-line holography. *J. Geophys. Res. Ocean* 117 (C5). doi: 10.1029/2011JC007613

Guerra, M., and Thomson, J. (2017). Turbulence measurements from five-beam acoustic doppler current profilers. *J. Atmos. Oceanic Technol.* 34, 1267–1284. doi: 10.1175/JTECH-D-16-0148.1

Hamm, C. E. (2002). Interactive aggregation and sedimentation of diatoms and clay-sized lithogenic material. *Limnol. Oceanogr.* 47, 1790–1795. doi: 10.4319/lo.2002.47.6.1790

Ho, Y., and Wookey, S. (2020). The real-world-weight cross-entropy loss function: modeling the costs of mislabeling. *IEEE Access* 8, 4806–4813. doi: 10.1109/ACCESS.2019.2962617

Jocher, G., Chaurasia, A., Stoken, A., and Borovec, J. (2022). *ultralytics/yolov5: v7.0 - YOLOv5 SOTA realtime instance segmentation*. doi: 10.5281/ZENODO.3908559

Johnson, Z. I., Zinser, E. R., Coe, A., McNulty, N. P., Woodward, E. M. S., and Chisholm, S. W. (2006). Niche partitioning among prochlorococcus ecotypes along ocean-scale environmental gradients. *Science* 311, 1737–1740. doi: 10.1126/science.1118052

Karp-Boss, L., and Jumars, P. A. (1998). Motion of diatom chains in steady shear flow. *Limnol. Oceanogr.* 43, 1767–1773. doi: 10.4319/lo.1998.43.8.1767

Kiko, R., Picheral, M., Antoine, D., Babin, M., Berline, L., Biard, T., et al. (2022). A global marine particle size distribution dataset obtained with the Underwater Vision Profiler 5. *Earth Syst. Sci. Data* 14, 4315–4337. doi: 10.5194/essd-14-4315-2022

Lin, T.-Y., Dollar, P., Girshick, R., He, K., Hariharan, B., and Belongie, S. (2017). "Feature pyramid networks for object detection," in *Proceedings of the IEEE conference on computer vision and pattern recognition (CVPR)*., 2117–2125. doi: 10.1109/CVPR.2017.106

Litchman, E., and Klausmeier, C. A. (2008). Trait-based community ecology of phytoplankton. *Annu. Rev. Ecol. Evol. Syst.* 39, 615–639. doi: 10.1146/annurev.ecolsys.39.110707.173549

Liu, S., Qi, L., Qin, H., Shi, J., and Jia, J. (2018). "Path aggregation network for instance segmentation," in *Proceedings of the IEEE conference on computer vision and pattern recognition (CVPR)*., 8759–8768. doi: 10.1109/CVPR.2018.00913

Liu, Z., Sarah, G., Tomoko, T., Thangavel, T., Marika, T., Nick, B., et al. (2023). "Advanced subsea imaging technique of digital holography: in *situ* measurement of marine microscale plankton and particles," in *2023 IEEE underwater technology (UT)*, Tokyo, Japan, 1–9. doi: 10.1109/UT49729.2023.10103440

Lund, J. W. G., Kipling, C., and Le Cren, E. D. (1958). The inverted microscope method of estimating algal numbers and the statistical basis of estimations by counting. *Hydrobiologia* 11, 143–170. doi: 10.1007/BF00007865

MacLeod, N., Benfield, M., and Culverhouse, P. (2010). Time to automate identification. *Nature* 467, 154–155. doi: 10.1038/467154a

Maggi, F. (2007). Variable fractal dimension: A major control for floc structure and flocculation kinematics of suspended cohesive sediment. *J. Geophys. Res.* 112, C07012. doi: 10.1029/2006JC003951

Maggi, F., Manning, A. J., and Winterwerp, J. C. (2006). Image separation and geometric characterisation of mud flocs. *J. Hydrol.* 326, 325–348. doi: 10.1016/j.jhydrol.2005.11.005

Many, G., Durrieu De Madron, X., Verney, R., Bourrin, F., Renosh, P. R., Jourdin, F., et al. (2019). Geometry, fractal dimension and settling velocity of flocs during flooding conditions in the Rhône ROFI. *Estuar. Coast. Shelf Sci.* 219, 1–13. doi: 10.1016/j.ecss.2019.01.017

Marcos, Seymour, J. R., Luhar, M., Durham, W. M., Mitchell, J. G., Macke, A., et al. (2011). Microbial alignment in flow changes ocean light climate. *Proc. Natl. Acad. Sci. U.S.A.* 108, 3860–3864. doi: 10.1073/pnas.1014576108

Martini, S., Larras, F., Boyé, A., Faure, E., Aberle, N., Archambault, P., et al. (2021). Functional trait-based approaches as a common framework for aquatic ecologists. *Limnol. Oceanogr.* 66, 965–994. doi: 10.1002/lno.11655

Mcgill, B., Enquist, B., Weiher, E., and Westoby, M. (2006). Rebuilding community ecology from functional traits. *Trends Ecol. Evol.* 21, 178–185. doi: 10.1016/j.tree.2006.02.002

Moran, M. A., Buchan, A., González, J. M., Heidelberg, J. F., Whitman, W. B., Kiene, R. P., et al. (2004). Genome sequence of Silicibacter pomeroyi reveals adaptations to the marine environment. *Nature* 432, 910–913. doi: 10.1038/nature03170

Musielak, M. M., Karp-Boss, L., Jumars, P. A., and Fauci, L. J. (2009). Nutrient transport and acquisition by diatom chains in a moving fluid. *J. Fluid Mech.* 638, 401–421. doi: 10.1017/S0022112009991108

Naselli-Flores, L., Padisák, J., and Albay, M. (2007). Shape and size in phytoplankton ecology: do they matter? *Hydrobiologia* 578, 157–161. doi: 10.1007/s10750-006-2815-z

Nayak, A. R., Malkiel, E., McFarland, M. N., Twardowski, M. S., and Sullivan, J. M. (2021). Review of holography in the aquatic sciences: *in situ* characterization of particles, plankton, and small scale biophysical interactions. *Front. Mar. Sci.* 7. doi: 10.3389/fmars.2020.572147

Nayak, A. R., McFarland, M. N., Sullivan, J. M., and Twardowski, M. S. (2018). Evidence for ubiquitous preferential particle orientation in representative oceanic shear flows. *Limnol. Oceanogr.* 63, 122–143. doi: 10.1002/lno.10618

Neubeck, A., and Van Gool, L. (2006). "Efficient non-maximum suppression," in *18th International Conference on Pattern Recognition (ICPR'06)*, Vol. 3, 850–855. doi: 10.1109/ICPR.2006.479

Orenstein, E. C., Ayata, S., Maps, F., Becker, É.C., Benedetti, F., Biard, T., et al. (2022). Machine learning techniques to characterize functional traits of plankton from image data. *Limnol. Oceanogr.* 67, 1647–1669. doi: 10.1002/lno.12101

Padilla, R., Netto, S. L., and Da Silva, E. A. B. (2020). "A survey on performance metrics for object-detection algorithms," in *2020 International Conference on Systems, Signals and Image Processing (IWSSIP)*, Niterói, Brazil., 237–242. doi: 10.1109/IWSSIP48289.2020.9145130

Padisak, J. (2003). Sinking properties of some phytoplankton shapes and the relation of form resistance to morphological diversity of plankton – an experimental study. *Hydrobiologia* 171, 243–257. doi: 10.1023/A:1024613001147

Pan, G., Chai, F., Tang, D., and Wang, D. (2017). Marine phytoplankton biomass responses to typhoon events in the South China Sea based on physical-biogeochemical model. *Ecol. Model.* 356, 38–47. doi: 10.1016/j.ecolmodel.2017.04.013

Passow, U. (2002). Transparent exopolymer particles (TEP) in aquatic environments. *Prog. Oceanogr.* 55, 287–333. doi: 10.1016/S0079-6611(02)00138-6

Prairie, J. C., Sutherland, K. R., Nickols, K. J., and Kaltenberg, A. M. (2012). Biophysical interactions in the plankton: A cross-scale review: Biophysical interactions in the plankton. *Limnol. Oceanogr. Fluids Environ.* 2, 121–145. doi: 10.1215/21573689-1964713

Redmon, J., and Farhadi, A. (2018). YOLOv3: an incremental improvement. doi: 10.48550/arXiv.1804.02767

Riato, L., Hill, R. A., Herlihy, A. T., Peck, D. V., Kaufmann, P. R., Stoddard, J. L., et al. (2022). Genus-level, trait-based multimetric diatom indices for assessing the ecological condition of rivers and streams across the conterminous United States. *Ecol. Indic.* 141, 109131. doi: 10.1016/j.ecolind.2022.109131

Sengupta, A., Carrara, F., and Stocker, R. (2017). Phytoplankton can actively diversify their migration strategy in response to turbulent cues. *Nature* 543, 555–558. doi: 10.1038/nature21415

Smith, W. A. M. N., Katz, J., and Osborn, T. R. (2005). On the structure of turbulence in the bottom boundary layer of the coastal ocean. *J. Phys. Oceanogr.* 35, 72–93. doi: 10.1175/JPO-2673.1

Stacey, M. T., McManus, M. A., and Steinbuck, J. V. (2007). Convergences and divergences and thin layer formation and maintenance. *Limnol. Oceanogr.* 52, 1523–1532. doi: 10.4319/lo.2007.52.4.1523

Stemmann, L., and Boss, E. (2012). Plankton and particle size and packaging: from determining optical properties to driving the biological pump. *Annu. Rev. Mar. Sci.* 4, 263–290. doi: 10.1146/annurev-marine-120710-100853

Takabayashi, M., Lew, K., Johnson, A., Marchi, A., Dugdale, R., and Wilkerson, F. P. (2006). The effect of nutrient availability and temperature on chain length of the diatom, Skeletonema costatum. *J. Plankton Res.* 28, 831–840. doi: 10.1093/plankt/fbl018

Tang, F. H. M., and Maggi, F. (2015). Reconstructing the fractal dimension of granular aggregates from light intensity spectra. *Soft Matter* 11, 9150–9159. doi: 10.1039/C5SM01885D

Terven, J., Córdova-Esparza, D.-M., and Romero-González, J.-A. (2023). A comprehensive review of YOLO architectures in computer vision: from YOLOv1 to YOLOv8 and YOLO-NAS. *Make* 5, 1680–1716. doi: 10.3390/make5040083

Trudnowska, E., Lacour, L., Ardyna, M., Rogge, A., Irisson, J. O., Waite, A. M., et al. (2021). Marine snow morphology illuminates the evolution of phytoplankton blooms and determines their subsequent vertical export. *Nat. Commun.* 12, 2816. doi: 10.1038/s41467-021-22994-4

Vahedi, A., and Gorczyca, B. (2011). Application of fractal dimensions to study the structure of flocs formed in lime softening process. *Water Res.* 45, 545–556. doi: 10.1016/j.watres.2010.09.014

Violle, C., Navas, M., Vile, D., Kazakou, E., Fortunel, C., Hummel, I., et al. (2007). Let the concept of trait be functional! *Oikos* 116, 882–892. doi: 10.1111/j.0030-1299.2007.15559.x

Wang, B., Chen, J., Jin, H., Li, H., Huang, D., and Cai, W. (2017). Diatom bloom-derived bottom water hypoxia off the Changjiang estuary, with and without typhoon influence. *Limnol. Oceanogr.* 62, 1552–1569. doi: 10.1002/lno.10517

Wang, C.-Y., Mark Liao, H.-Y., Wu, Y.-H., Chen, P.-Y., Hsieh, J.-W., and Yeh, I.-H. (2020). "CSPNet: A new backbone that can enhance learning capability of CNN," in *Proceedings of the IEEE/CVF conference on computer vision and pattern recognition workshops (CVPRW)*., 1571–1580. doi: 10.1109/CVPRW50498.2020.00203

Worden, A. Z., Follows, M. J., Giovannoni, S. J., Wilken, S., Zimmerman, A. E., and Keeling, P. J. (2015). Rethinking the marine carbon cycle: Factoring in the multifarious lifestyles of microbes. *Science* 347, 1257594. doi: 10.1126/science.1257594

Young, A. M., Karp-Boss, L., Jumars, P. A., and Landis, E. N. (2012). Quantifying diatom aspirations: Mechanical properties of chain-forming species. *Limnol. Oceanogr.* 57, 1789–1801. doi: 10.4319/lo.2012.57.6.1789

Zheng, Z., Wang, P., Liu, W., Li, J., Ye, R., and Ren, D. (2020). Distance-ioU loss: faster and better learning for bounding box regression. *AAAI* 34, 12993–13000. doi: 10.1609/aaai.v34i07.6999